CHAPTER IV

Analytical Approach

This dissertation included two numerical methods for the analysis and predicted behavior of the experimental specimens. One method was based on the finite difference method and the other was based on a finite element method. A finite difference method was used for determining the capacity of specimens for setting up a test program. This method was simple and readily gave results based on approximating and simplifying assumptions. The finite element method which including a concrete plastic model, was performed to more closely study the behavior of spirally confined concrete. Using a system identification approach, a concrete model was calibrated by adjusting plastic parameters to correspond to known triaxial behavior. Subsequently the finite element model was compared to the test results to confirm that the concrete plastic model could be used for parametric studies. The details of the analytical work are presented in this chapter.

4.1 Finite Difference Analysis

The finite difference analysis (FDA) consists of transforming a governing partial differential equation into difference equations over a sub-divided domain.

To use a finite difference method to attempt to solve (or, more generally, to approximate the solution to) a problem, the applicable domain is discretized into conveniently small intervals. This is usually done by dividing the domain into a uniform grid such as illustrated in Figure 4.1. In this way, finite difference methods produce sets of discrete numerical approximations to the derivatives of the governing equation at discrete points.

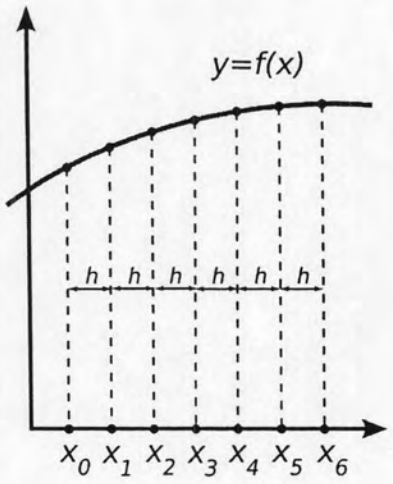

Figure 4.1 Discretization of a domain

Finite difference methods approximate the solutions to differential equations by replacing derivative expressions with approximately equivalent difference quotients. That is, because the first derivative of a function f is, by definition,

$$f'(a) = \lim_{h \to 0} \frac{f(a+h) - f(a)}{h}, \tag{4.1}$$

then a reasonable approximation for that derivative would be to take

$$f'(a) \approx \frac{f(a+h) - f(a)}{h}, \tag{4.2}$$

for some small value of h.

In fact, this is the forward difference equation for the first derivative. Using this and similar formulae to replace derivative expressions in differential equations, approximate solutions can be solved by simple arithmetic procedures.

To discretize a specimen model, section parameters were set as shown in Figure 4.2.

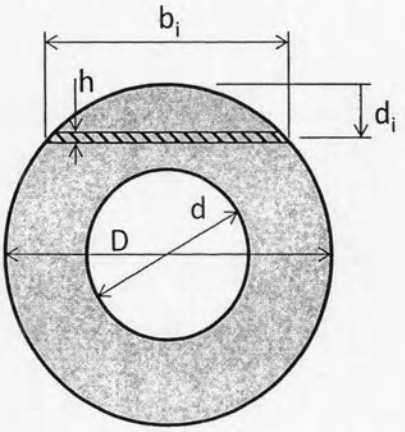

Figure 4.2 Section parameters

In this figure,

$$b_i = \begin{cases} 2\sqrt{\left(\frac{D}{2}\right)^2 - \left(\frac{D}{2} - d_i\right)^2} & ; \frac{D}{2} + d \le d_i \le \frac{D}{2} - d \quad (4.3) \\ 2\left[\sqrt{\left(\frac{D}{2}\right)^2 - \left(\frac{D}{2} - d_i\right)^2} - \sqrt{\left(\frac{d}{2}\right)^2 - \left(\frac{D}{2} - d_i\right)^2}\right] & ; d_i < \frac{D}{2} + d \quad (4.4) \end{cases}$$

Utilizing the finite difference method to determine the capacity of specimens, proper assumptions have to be setup for representing confinement effects. For a concrete model, a tri-axially stressed concrete model by Richart was applied for the material model of concrete. The assumed concrete model is stated below:

$$f_{ci} = f'_{cc}\left(\frac{2\varepsilon_{ci}}{\varepsilon_{co}} - \left(\frac{\varepsilon_{ci}}{\varepsilon_{co}}\right)^2\right) \quad (4.5)$$

where

$$f'_{cc} = f'_c + 4.1 f_l$$

A Hognestaad concrete model as a basis function, ε_{co} can be assumed = 0.002 and f_l can be calculated as shown in equation (2.2).

This test used the DSI-America Monostrand® post-tensioning system that is an unbonded-type. Thus, for a prestressed steel model, strain along a strand can be assumed as uniformly equal strain all over a strand length. And because of a

specimen length was very short (depth/span ratio =2), curvature due to loading is very small and can be neglected for simplicity.

To determine the $M-\phi$ diagram and the $P-M$ diagram, the two variables for this problem are ε_c and c. Therefore, equilibrium equations are set up as stated below:

$$\sum F = \sum_{i=0}^{c} (f_{ci} b_i h) - nF_{ps} \cos 45° - P_r = 0 \tag{4.6}$$

$$\sum M = \sum_{i=0}^{c} (f_{ci} b_i h d_i) - M_r = 0 \tag{4.7}$$

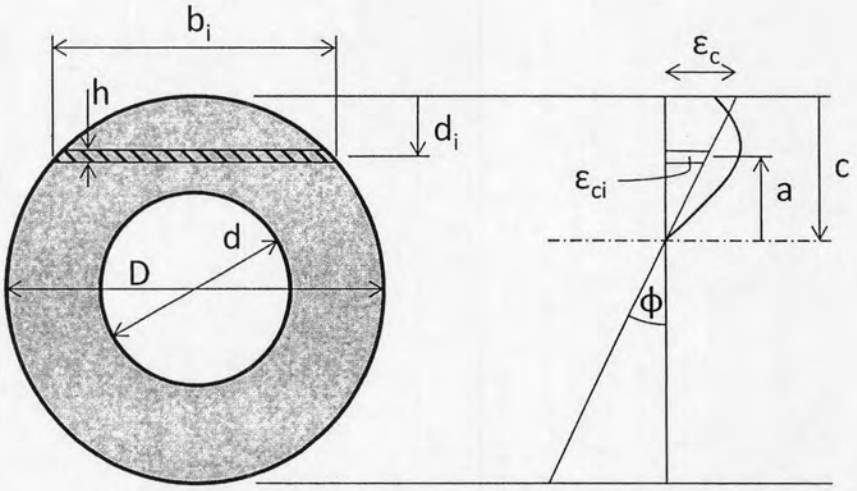

Figure 4.3 Strain compatibility

From strain compatibility as illustrated in Figure 4.3, ε_c and c are varied to find $M-\phi$ and for $\varepsilon_c = \varepsilon_{cu}$, varying c results in the $P-M$ diagram. After calculating by following this procedure, the results are illustrated in Figure 4.4 and Figure 4.5.

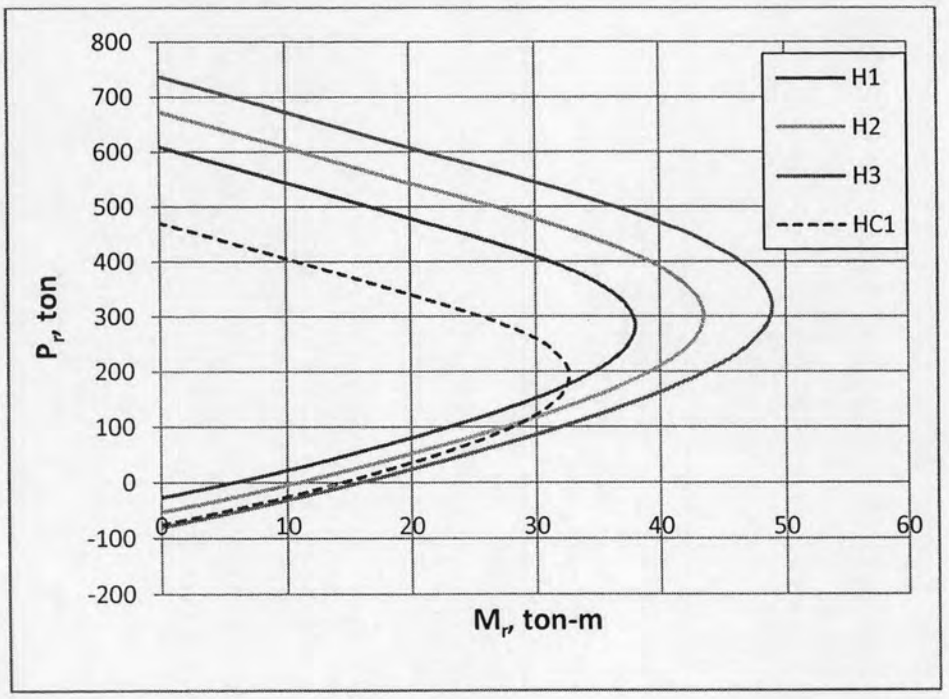

Figure 4.4 $P - M$ diagram of test specimens

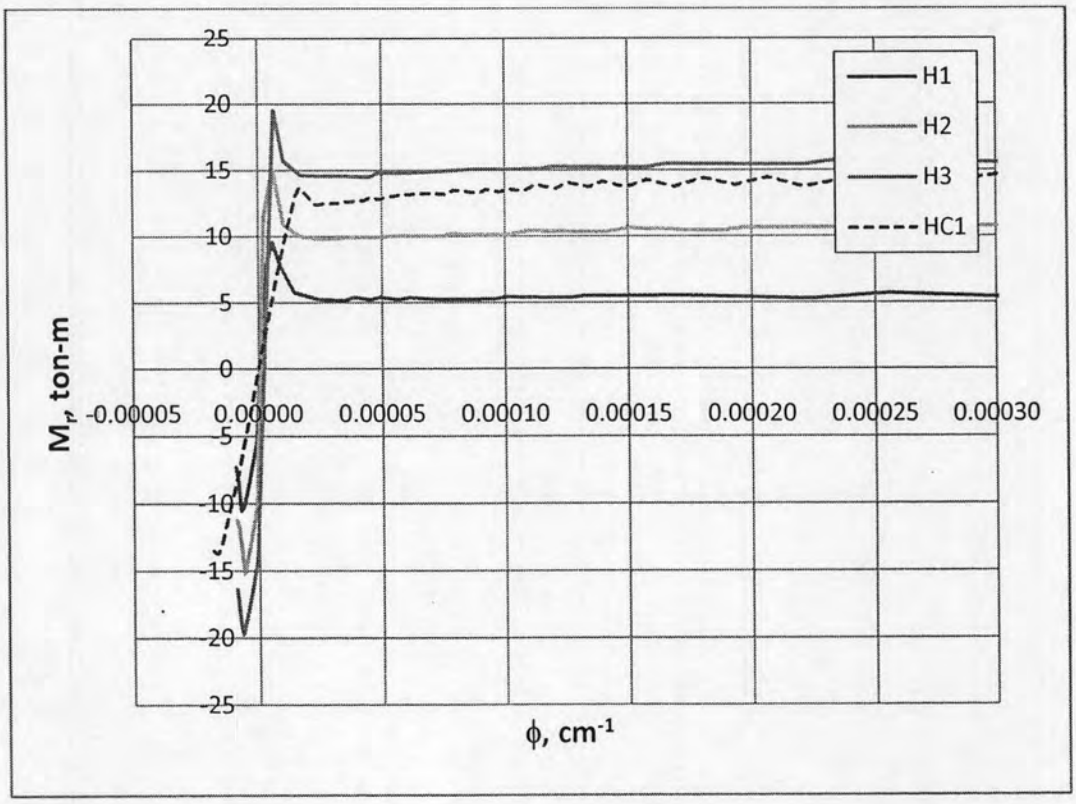

Figure 4.5 $M - \phi$ diagram for design specimens

Load resistance can be calculated by converting the resisting moment. Elastic theory can be applied to analyze the ultimate load resistance since specimens were brittle and stiffness did not change significantly up to ultimate. Thus, load resistances can be calculated as shown below:

$$P_r = \frac{4M_r}{L} \tag{4.8}$$

Table 4.1 Compare calculated ultimate capacity from FDM to the test results

Specimen	Ultimate Capacity from test (tons)	Calc'd. Ultimate Capacity, FDM (tons)
H1	39.83	46.59
H2	43.49	63.78
H3	48.36	85.35
HC1	29.72	57.04

The difference between test results and calculated results is related to the assumptions of the concrete confinement model as represented by a tri-axially stressed concrete model. Additionally, the complex shear fields were not accounted for in the finite difference analysis. Despite these approximations, it was felt that the results were adequate for preliminary design considerations including the estimation of the hydraulic jack capacity required.

4.2 Finite Element Analysis

From finite difference analysis results, further light was shed on an appropriate material model for tri-axially stressed concrete. Realistic confinement effects of spiral post-tensioning and shear effects from depth-to-span ratios ($D/L = 0.5$) were not included the in finite difference analysis. Thus, finite element

analysis was used to include more complex effects such as those related to the use of a confinement spiral post-tensioning system.

4.2.1 Finite Element Analysis of Confined Concrete

There are three main reasons for using the finite element method. Firstly it was used to verify the confinement behavior of a concrete plastic model by modeling triaxial behavior and comparing the result with the existing proposed experimental model by Richart. Secondly, the verified concrete plastic model was applied to the specimen models to confirm that a concrete plastic model is applicable for spiral post-tensioning systems. The use of finite element method was also confirmed in comparison with experimental results performed in this dissertation. In the third case it was necessary to achieve a structural model for spirally prestressed concrete by performing parametric studies on axial tests under spirally prestressed confinement. Due to constraints of equipment and time, laboratory tests corresponding to axially loaded specimens were not conducted.

Since, in this analysis, stiffness is a function of displacements material non-linearity becomes a consideration. Thus, in structural equations;

$$\{K\}\{D\} = \{R\} \tag{4.9}$$

The coefficient matrix $\{K\}$ becomes functions of $\{D\}$. We cannot immediately solve for $\{D\}$ because information needed to construct $\{K\}$ and $\{R\}$ is not known in advance. An iterative process is required to obtain $\{D\}$ and its associated $\{K\}$ and $\{R\}$ such that the product $\{K\}\{D\}$ is in equilibrium with $\{R\}$.

When equations $\{K\}\{D\} = \{R\}$ are nonlinear the principle of superposition does not apply. That is, we cannot scale results in proportion to load or superpose results of different load cases. Each different load case requires a separate analysis. Also, for a given set of loads there may be more than one solution $\{D\}$. If a load case consists of two portions that are sequentially applied, reversing the sequence of application may produce different results.

Prior to any yielding, many materials display almost linear and elastic response, so that stresses can be calculated by knowing elastic constants and strains. When there is yielding, not only are load, deformation, and stress nonlinearly related, they are also history-dependent. That is, changing the load history path to a particular final load state is likely to change final results. For an arbitrary load history, the final state of stress and deformation can be determined only by accounting for the history of stress and strain. In calculation, history is taken into account by formulations that relate increments of stress to increments of strain. In this section we summarize such a formulation in sufficiently general terms that it can be applied to concrete materials as stated below.

Uniaxial Tension and Compression Stress Behavior

The model assumes that the uniaxial tensile and compressive response of concrete is characterized by plasticity, as shown in Figure 4.6.

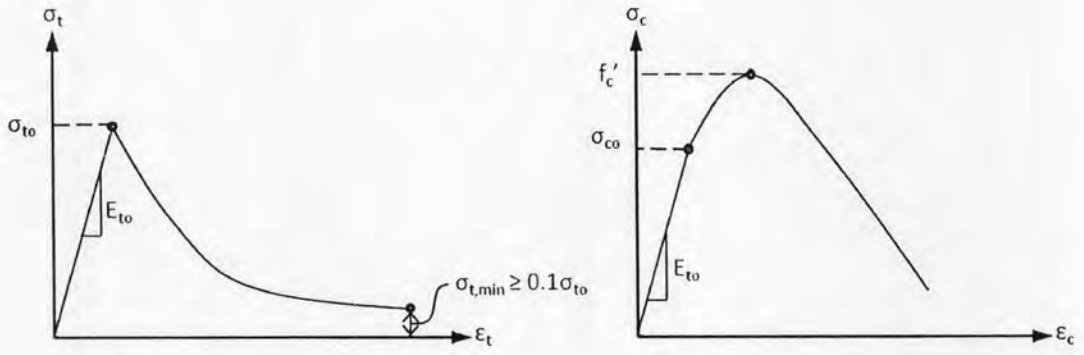

(a) (b)

Figure 4.6 Response of concrete to uniaxial loading in a) tension and b) compression

Under uniaxial tension the stress-strain response follows a linear elastic relationship until the value of the failure stress, σ_{to}, is reached. The failure stress corresponds to the onset of micro-cracking in the concrete material. Beyond the failure stress the formation of micro-cracks is represented macroscopically with a softening stress-strain response, which induces strain localization in the concrete structure. Under uniaxial compression the response is linear (with stiffness of initial tangent modulus of elasticity, E_{to}) until the value of initial yield, σ_{co} is reached. In

the plastic regime the response is typically characterized by stress hardening followed by strain softening beyond the ultimate stress, f_c'. This representation, although somewhat simplified, captures the main features of the response of concrete.

Effective Stress Invariants

The effective stress is defined as:

$$\overline{\boldsymbol{\sigma}} = \boldsymbol{D}_o^{el} : (\boldsymbol{\varepsilon} - \boldsymbol{\varepsilon}^{pl}) \tag{4.10}$$

The plastic flow potential function and the yield surface make use of two stress invariants of the effective stress tensor, namely the hydrostatic pressure stress,

$$\overline{p} = -\frac{1}{3}\mathrm{trace}(\overline{\boldsymbol{\sigma}}) \tag{4.11}$$

and the Mises equivalent effective stress,

$$\overline{q} = \sqrt{\frac{3}{2}\left(\overline{\mathbf{S}} : \overline{\mathbf{S}}\right)} \tag{4.12}$$

where $\overline{\mathbf{S}}$ is the effective stress deviator, defined as

$$\overline{\mathbf{S}} = \overline{\boldsymbol{\sigma}} + \overline{p}\mathbf{I} \tag{4.13}$$

Plastic flow

The rule of plastic flow is governed by a flow potential *G* according to the flow rule:

$$\dot{\boldsymbol{\varepsilon}}^{pl} = \dot{\lambda}\frac{\partial G(\overline{\boldsymbol{\sigma}})}{\partial \overline{\boldsymbol{\sigma}}}$$

The concrete plastic model assumes nonassociated potential plastic flow. The flow potential *G* used for this model is the Drucker-Prager hyperbolic function:

$$G = \sqrt{(\epsilon \sigma_{to} \tan\psi)^2 + \overline{q}^2} - \overline{p}\tan\psi \tag{4.14}$$

where,

$\psi(\theta, f_i)$	is the dilation angle measured in the $p-q$ plane at high confining pressure;
$\sigma_{to}(\theta, f_i) = \sigma_t\|_{\tilde{\varepsilon}_t^{pl}=0, \dot{\tilde{\varepsilon}}_t^{pl}=0}$	is the uniaxial tensile stress at failure, taken from the user-specified tension stiffening data;
$\epsilon(\theta, f_i)$	is a parameter, referred to as the eccentricity, that defines the rate at which the function approaches an asymptotic level (the flow potential tends to a straight line as the eccentricity tends to zero)

This flow potential, which is continuous and smooth, ensures that the flow direction is always uniquely defined. The function approaches the linear Drucker-Prager flow potential asymptotically at high confining pressure stress and intersects the hydrostatic pressure axis at 90°.

The default flow potential eccentricity is $\epsilon = 0.1$, which implies that the material has almost the same dilation angle over a wide range of confining pressure stress values. Increasing the value of ϵ provides more curvature to the flow potential, implying that the dilation angle increases more rapidly as the confining pressure decreases. Values of ε that are significantly lower than the default value may lead to convergence problems if the material is subjected to low confining pressures because of the very tight curvature of the flow potential locally where it intersects the p-axis.

Yield function

The model makes use of the yield function of Lubliner et. al.[8] (1989), with the modifications proposed by Lee and Fenves[9] (1998) to account for different evolution

[8] Lubliner, J., J. Oliver, S. Oller, and E. Oñate, "A Plastic-Damage Model for Concrete," International Journal of Solids and Structures, vol. 25, pp. 299–329, 1989.

of strength under tension and compression. The evolution of the yield surface is controlled by the hardening variables, $\tilde{\varepsilon}_t^{pl}$ and $\tilde{\varepsilon}_c^{pl}$. In terms of effective stresses, the yield function takes the form

$$F = \frac{1}{1-\alpha}\left(\bar{q} - 3\alpha\bar{p} + \beta(\tilde{\varepsilon}^{pl})\langle\hat{\bar{\sigma}}_{\max}\rangle - \gamma\langle-\hat{\bar{\sigma}}_{\max}\rangle\right) - \bar{\sigma}_c\left(\tilde{\varepsilon}_c^{pl}\right) = 0$$

with,

$$\alpha = \frac{(\sigma_{bo}/\sigma_{co})-1}{2(\sigma_{bo}/\sigma_{co})-1}; 0 \le \alpha \le 0.5$$

$$\beta = \frac{\bar{\sigma}_c\left(\tilde{\varepsilon}_c^{pl}\right)}{\bar{\sigma}_t\left(\tilde{\varepsilon}_t^{pl}\right)}(1-\alpha) - (1+\alpha)$$

$$\gamma = \frac{3(1-K_c)}{2K_c-1}$$

Here,

The Macauley bracket $\langle\cdot\rangle$ is defined by $\langle x\rangle = \frac{1}{2}(|x| - x)$

$\hat{\bar{\sigma}}_{\max}$	is the maximum principal effective stress
σ_{bo}/σ_{co}	is the ratio of initial equibiaxial compressive yield stress to initial uniaxial compressive yield stress (a suitable value for concrete is 1.16)
K_c	is the ratio of the second stress invariant on the tensile meridian, $q_{(\mathrm{TM})}$, to that on the compressive meridian, $q_{(\mathrm{CM})}$, at initial yield for any given value of the pressure invariant p such that the maximum principal stress is negative, $\hat{\sigma}_{\max} < 0$ as shown in Figure 4.7 and must satisfy the condition $0.5 < K_c \le 1.0$ (an appropriate value for concrete as used in this thesis is $2/3$)
$\bar{\sigma}_t\left(\tilde{\varepsilon}_t^{pl}\right)$	is the effective tensile cohesion stress
$\bar{\sigma}_c\left(\tilde{\varepsilon}_c^{pl}\right)$	is the effective compressive cohesion stress

[9] Lee, J., and G. L. Fenves, "Plastic-Damage Model for Cyclic Loading of Concrete Structures," Journal of Engineering Mechanics, vol. 124, no.8, pp. 892–900, 1998.

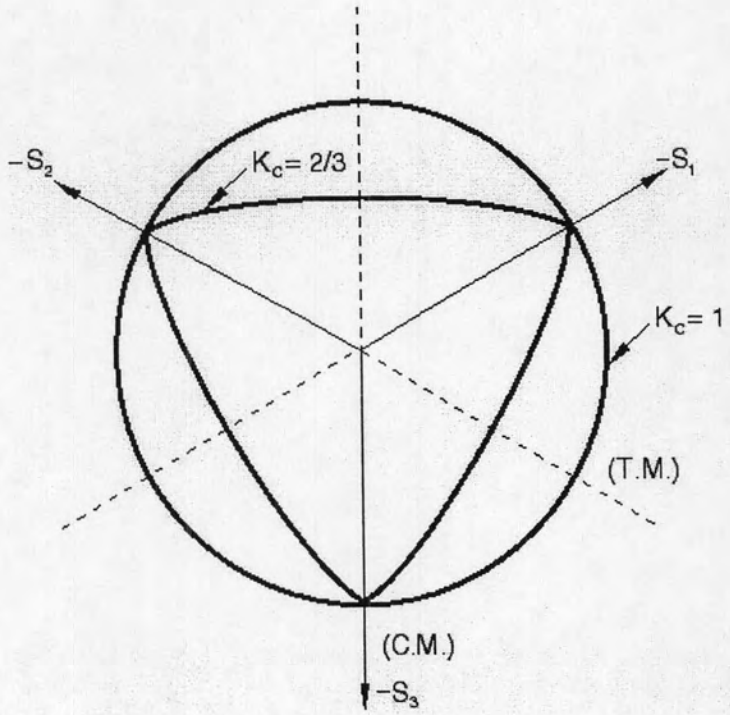

Figure 4.7 Yield surfaces in the deviatoric plane, with various values of K_c

Typical yield surfaces are shown in Figure 4.7 on the deviatoric plane and in Figure for plane stress conditions.

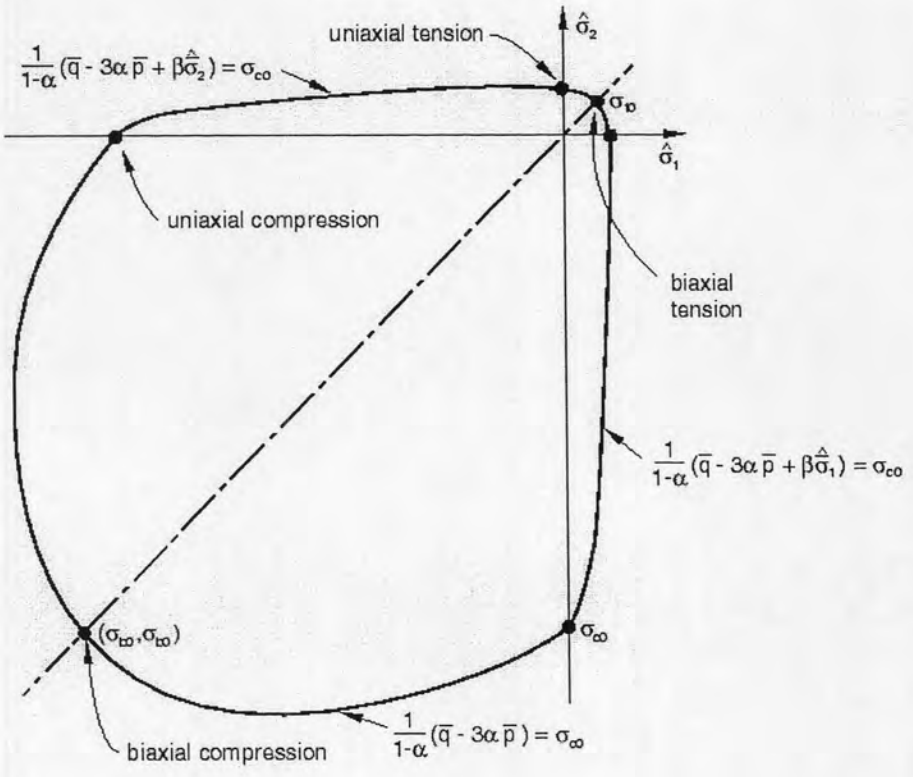

Figure 4.8 Yield surface in plane stress

Visualization of Crack Directions

Unlike concrete models based on the smeared crack approach, the concrete plastic model does not have the notion of cracks developing at the material integration point. However, it is possible to introduce the concept of an effective crack direction with the purpose of obtaining a graphical visualization of the cracking patterns in the concrete structure. Following Lubliner et. al. (1989), we can assume that cracking initiates at points where the tensile equivalent plastic strain is greater than zero, $\tilde{\varepsilon}_t^{pl} > 0$, and the maximum principal plastic strain is positive. The direction of the vector normal to the crack plane is assumed to be parallel to the direction of the maximum principal plastic strain.

4.2.2 Modeling of Triaxial Test

Utilizing a plastic concrete model as a material model for a triaxial test, the mesh geometry and load pattern are illustrated in Figure 4.9.

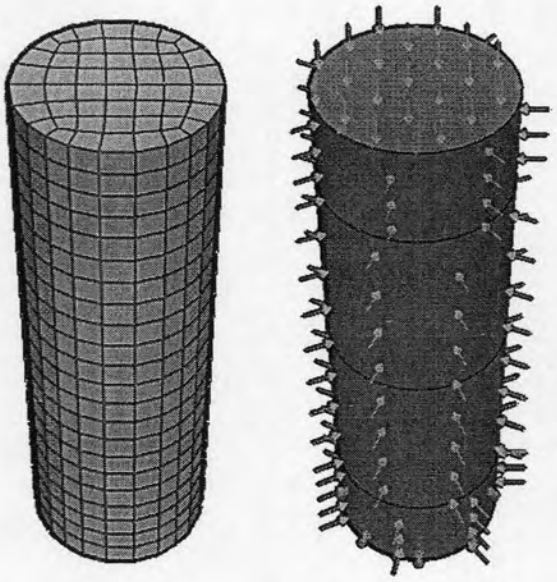

Figure 4.9 Mesh geometry and load pattern

By varying uniaxial strength of concrete (300 ksc, 450 ksc and 600 ksc) with various level of confined pressure, a plastic concrete model under triaxial stress behaves axially in terms of stress, σ_{zz} and plastic strain, ε_{zz}^{pl} as shown in Figure 4.10.

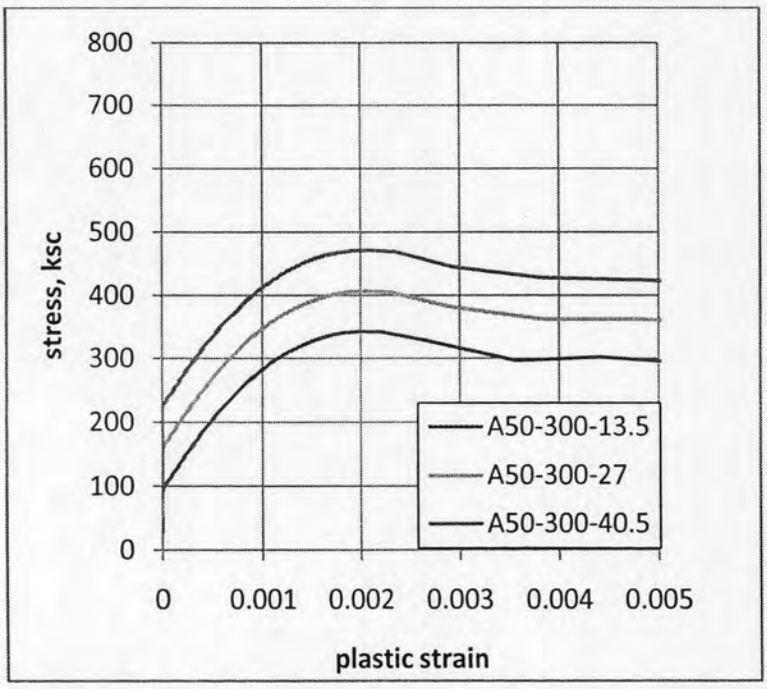

Figure 4.10a Stress-plastic strain relations of concrete with $f_c' = 300$ ksc under confined pressure of 13.5 ksc, 27 ksc, and 40.5 ksc

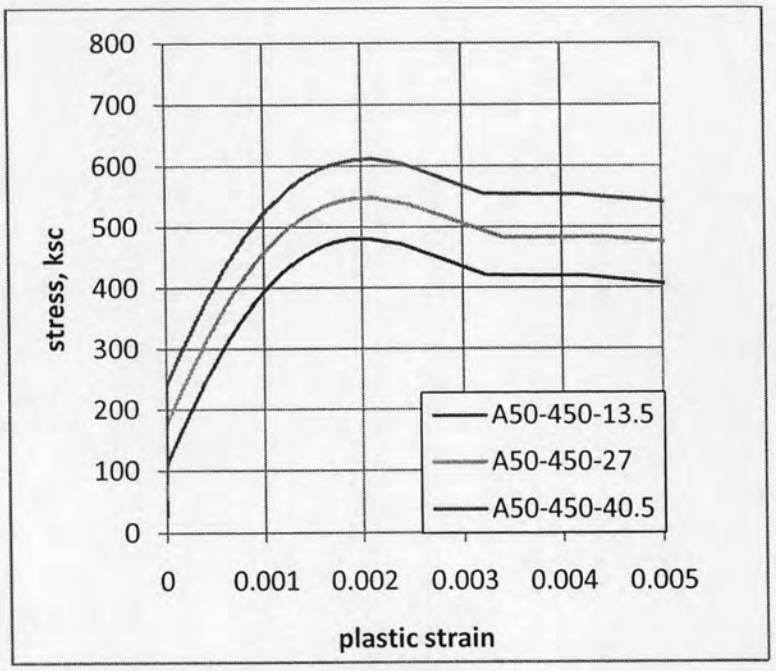

Figure 4.10b Stress-plastic strain relations of concrete with $f_c' = 450$ ksc under confined pressure of 13.5 ksc, 27 ksc, and 40.5 ksc

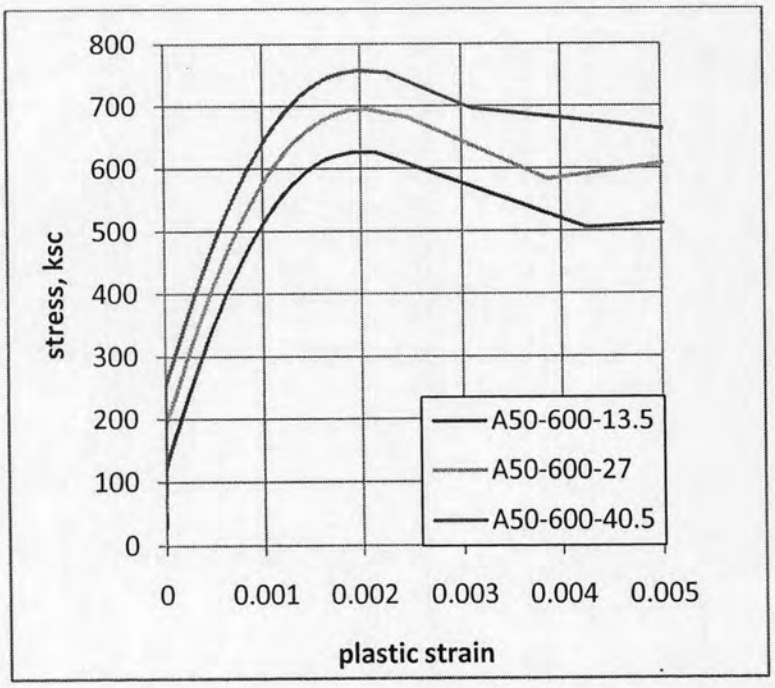

Figure 4.10c Stress-plastic strain relations of concrete with $f_c' = 600$ ksc under confined pressure of 13.5 ksc, 27 ksc, and 40.5 ksc

Plastic strain can be converted to total strain as illustrated in Figure 4.11. The following results show uniaxial strength of concrete under various levels of

hydrostatic pressure. In Figure 4.11, they also provide curve fitting equations of Hognestaad's concrete model for the relationship.

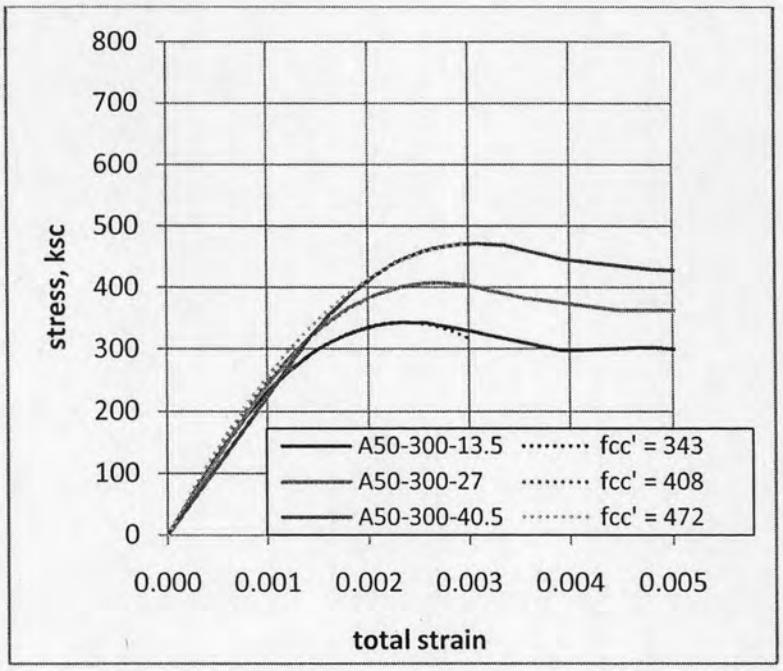

Figure 4.11a Stress-total strain relations of concrete with $f_c' = 300$ ksc under confined pressure of 13.5 ksc, 27 ksc and 40.5 ksc

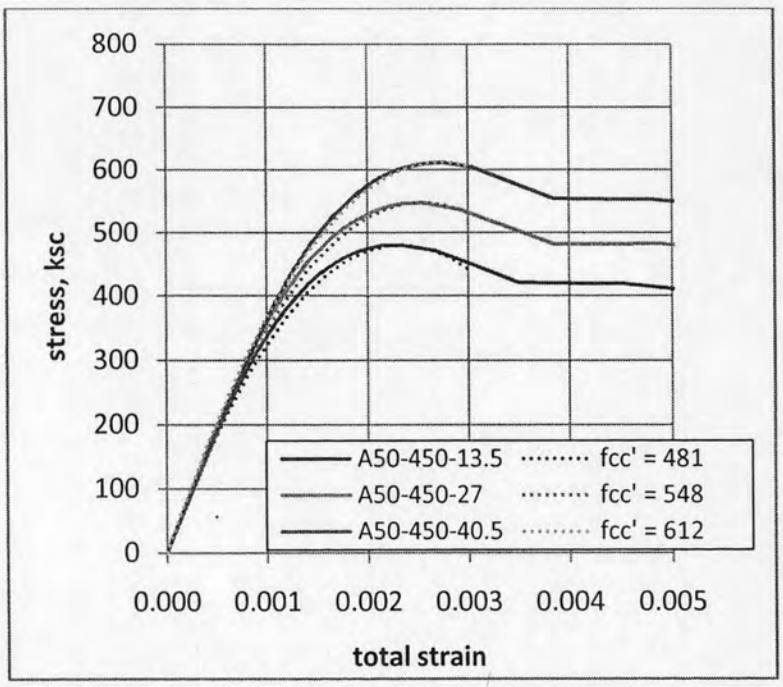

Figure 4.11b Stress-total strain relations of concrete with $f_c' = 450$ ksc under confined pressure of 13.5 ksc, 27 ksc and 40.5 ksc

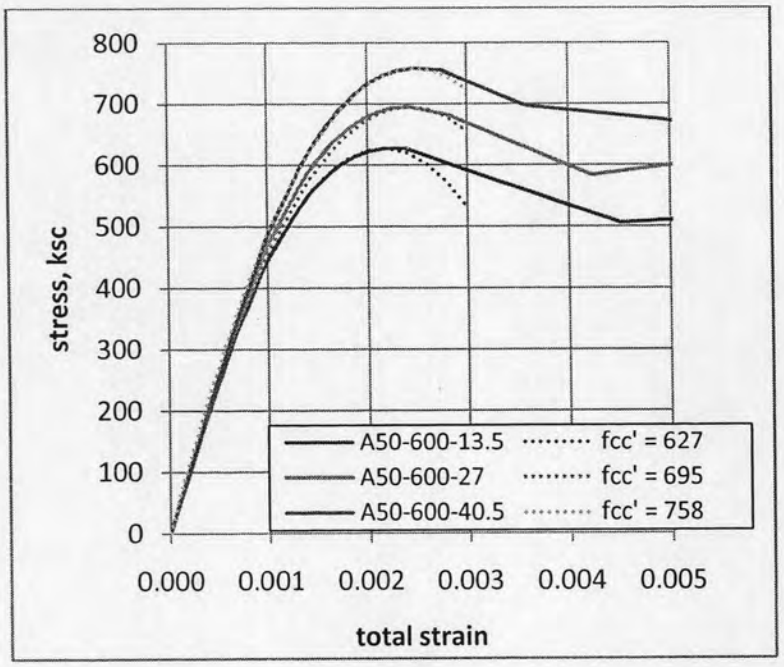

Figure 4.11c Stress-total strain relations of concrete with $f_c' = 600$ ksc under confined pressure of 13.5 ksc, 27 ksc and 40.5 ksc

All data can be summarized by a simply formula, $f_{cc}' = f_c' + k_c f_l$, and k_c can be calculated by $k_c = \frac{f_{cc}' - f_c'}{f_l}$. The results are compared as shown in Figure 4.12 with the previous proposed tri-axial concrete model shown in Table 2.1.

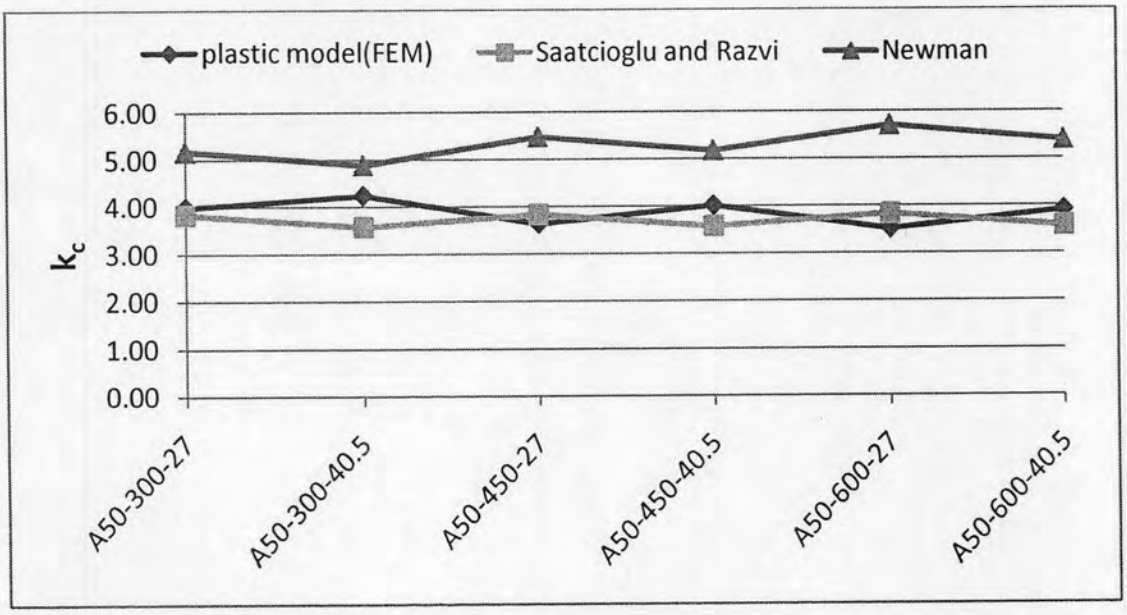

Figure 4.12 Comparison of k_c from plastic model to the previously proposed tri-axial concrete model

The values of k_c from the plastic concrete model vary around the values of the previously proposed model. Since k_c varies proportional to f_c' and f_l , the variation of k_c is predictable and the concrete plastic model is suitable as a concrete material model for use in a finite element analysis.

4.2.3 Modeling of Test Specimens

A verified and suitable concrete plastic model was applied to finite element analysis to confirm the test results. Due to geometrical complexities, the model was simplified to investigate the effects of confinement in accounting for concrete plastic material behavior under simple confining represented as pressure loads along the strands aligned on the outside surface of the thick-walled concrete pipe as illustrated in Figure 4.13. The magnitudes of pressure loads can be calculated as shown in equation (2.10) and are assumed to be averaged as uniform pressure all over the specimens as shown in Figure 2.2.

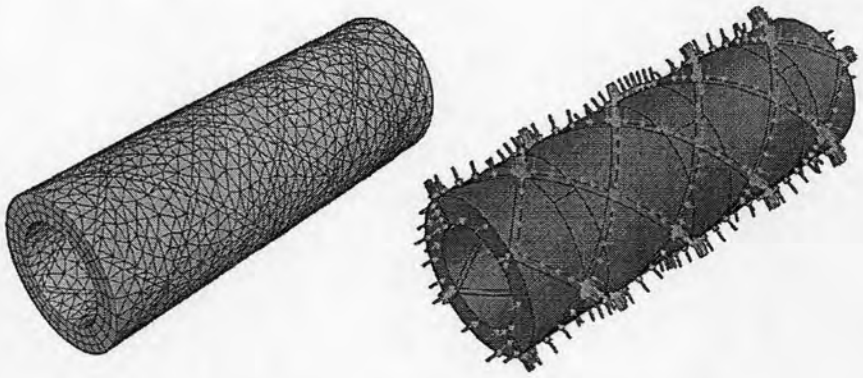

Figure 4.13 Mesh geometry and loading pattern

Due to the complex geometry, a suitable element for this model was determined to be a 6-node linear triangular prism element as illustrated in Figure 4.14. Load patterns separate into two steps. In the first step, loading was in the lateral direction along strand alignment as well as at both ends to simulate a prestressing sequence. A second load step included point loading at mid-span to simulate the corresponding experimental procedure.

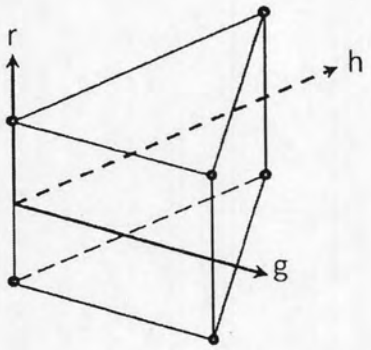

Figure 4.14 6-node linear triangular prism element

The uniaxial stress-strain relation for concrete was determined experimentally from cylinder compression tests and beam tension tests as shown in Figure 3.7 and Table 3.2.

The results from the finite element analysis were plotted and compared to the experimental results as shown in Figure 4.15. Stiffnesses in the elastic range from the finite element analysis results are similar since the plastic response was not included at that point. The stiffness of all specimens corresponded to the initial tangent modulus of elasticity, E_t. As plastic response is approached the concrete began to yield and the confining stress action began to be mobilized and thus affected the stiffnesses of the specimens.

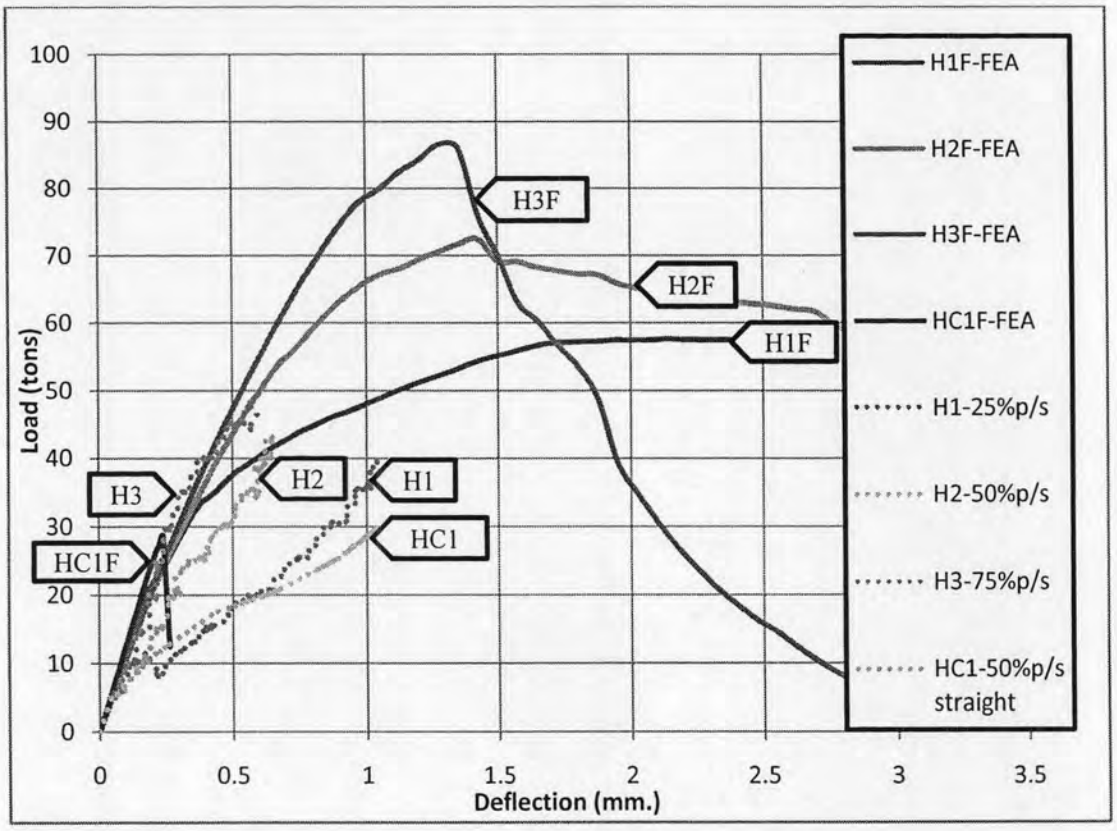

Figure 4.15 Load vs deflection curves from FEM compare to the test results

A comparison of results shows that the ultimate capacities determined from finite element analysis are close to those determined using the finite difference analysis. However, except for the control specimen HC1 for which ultimate strength predictions are similar, neither of the analyses give results that agree with the experimental results. It is felt, however, that while the finite element model is valid in handling the combined stresses due to prestressing and loading, it over predicts test results. It is strongly believed, and close inspection of test results support it, that the significant deviations of test predictions above actual test results are due to premature local concrete failure caused by the intense localized pressures exerted by the prestressing cables on the concrete. This effect could not be adequately modeled by the finite element model.

Table 4.2 Comparison of calculated ultimate capacity with test results

Specimen	Ultimate Capacity from test (tons)	Calc'd. Ultimate Capacity from FEM (tons)	Calc'd. Ultimate Capacity from FDM (tons)	Ratio of predicted by FEM to test result	Ratio of predicted by FDM to test result
H1	39.83	57.57	46.59	1.45	1.17
H2	43.49	72.49	63.78	1.67	1.47
H3	48.36	86.56	85.35	1.79	1.76
HC1	29.72	28.62	57.04	0.96	1.92

It should be noted that the laboratory tests did not represent the direct response to axial load of the active confinement of the spiral post-tensioning system. The tests performed represented indirect evaluation of active confinement behavior by subjecting simply-supported beam specimens to mid-span point loading. Due to the limitation of specimen size and loading equipment, direct axial compression tests on cylindrical concrete members could not be performed. However, evaluation of the beneficial confinement and shear strength enhancement of spiral prestressing strands was validated.

As discussed in chapter 3, the finite element analysis results failed to correspond favorably with test results. This was due to the complex overlapping of stress fields in the specimens as well as to the highly localized and intense stresses between the tendons and the concrete. Additionally, these stresses increased with applied loading and resulted in localized failure along the tendons. This local failure phenomenon was noted for all specimens.

General observations reveal that the ultimate strength results from finite element analysis and those from the experimental results increase correspondingly

with increased levels of confining prestress. As pointed out, however, the ultimate strength values of theoretical and experimental results do not correspond well due to local failure phenomena. Stress field overlapping, as well as non-compliant assumptions of modeling.

Despite these adverse developments between theory and experiment, it is felt that the finite element analysis would be better suited for predicting the behavior of axially loaded specimens that are spirally prestressed. This observation is used to justify a parametric study as presented below for axially loaded specimens.

4.2.4 Modeling of Uniaxial compression Tests

The plastic concrete model combined with a simplified model as previously mentioned, was used to analyze specimens subjected to a loading pattern and loading sequence as illustrated as in Figure 4.16.

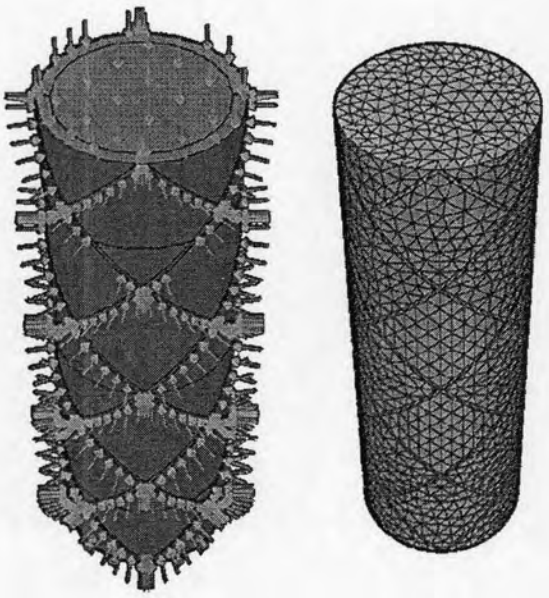

Figure 4.16a Loading pattern and mesh geometry for 8-strand specimen

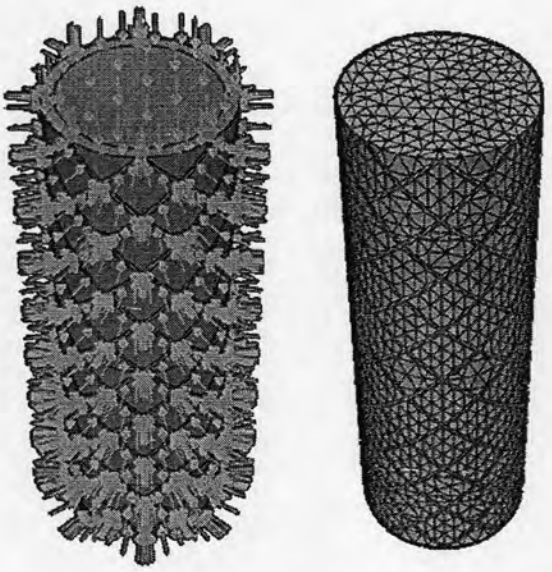

Figure 4.16b Loading pattern and mesh geometry for 16-strand specimen

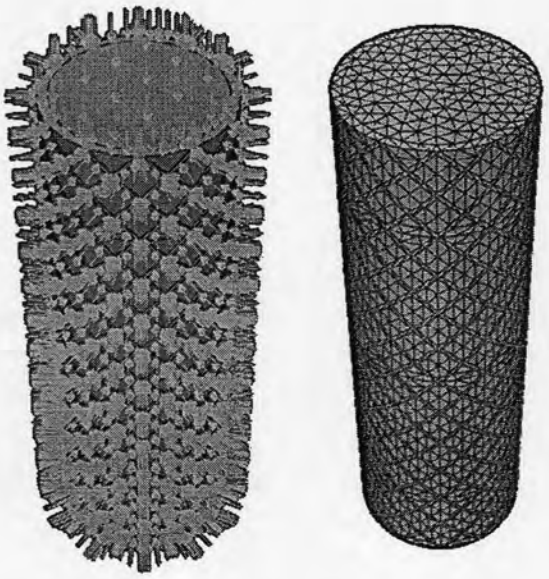

Figure 4.16c Loading pattern and mesh geometry for 24-strand specimen

Prestressing forces were first applied both laterally as confining stresses and longitudinally in compression as calculated. Loading was applied in the axial direction to simulate a uniaxial compression test. A 10-node modified quadratic tetrahedron element was used to model the complicated configuration and nonlinear geometry as shown in Figure 4.17.

The results of the uniaxial compression tests from finite element analysis represent an active confined concrete model with a spirally prestressed system. This model was applied for a parametric study and the results are presented and discussed in the next chapter.

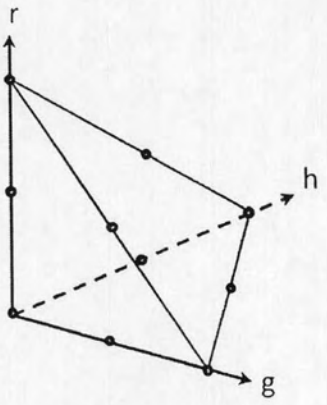

Figure 4.17 10-node modified quadratic tetrahedron element